Stem Cell Research & Therapy

RESEARCH Open Access

Mesenchymal stem cell-derived extracellular vesicles mitigate neuronal damage from intracerebral hemorrhage by modulating ferroptosis

Yanping Yang[1†], Lingfeng Gao[1†], Junxiu Xi[1,2†], Xiaoyan Liu[1,2], Hao Yang[1,2], Qiang Luo[1], Fei Xie[1], Jinyun Niu[3], Panpan Meng[1], Xiao Tian[1], Xiaoping Wu[4] and Qianfa Long[1,2*]

Abstract

Background Hemorrhagic stroke is a devastating cerebrovascular event with a high rate of early mortality and long-term disability. The therapeutic potential of mesenchymal stem cell-derived extracellular vesicles (MSC-EVs) for neurological conditions, such as intracerebral hemorrhage (ICH), has garnered considerable interest, has garnered considerable interest, though their mechanisms of action remain poorly understood.

Methods EVs were isolated from human umbilical cord MSCs, and SPECT/CT was used to track the ^{99m}Tc-labeled EVs in a mouse model of ICH. A series of comprehensive evaluations, including magnetic resonance imaging (MRI), histological study, RNA sequencing (RNA-Seq), or miRNA microarray, were performed to investigate the therapeutic action and mechanisms of MSC-EVs in both cellular and animal models of ICH.

Results Our findings show that intravenous injection of MSC-EVs exhibits a marked affinity for the ICH-affected brain regions and cortical neurons. EV infusion alleviates the pathological changes observed in MRI due to ICH and reduces damage to ipsilateral cortical neurons. RNA-Seq analysis reveals that EV treatment modulates key pathways involved in the neuronal system and metal ion transport in mice subjected to ICH. These data were supported by the attenuation of neuronal ferroptosis in neurons treated with Hemin and in ICH mice following EV therapy. Additionally, miRNA microarray analysis depicted the EV-miRNAs targeting genes associated with ferroptosis, and miR-214-3p was identified as a regulator of neuronal ferroptosis in the ICH cellular model.

Conclusions MSC-EVs offer neuroprotective effects against ICH-induced neuronal damage by modulating ferroptosis highlighting their therapeutic potential for combating neuronal ferroptosis in brain disorders.

Keywords Extracellular vesicles, Ferroptosis, miR-214-3P, Neuronal damage, Intracerebral hemorrhage

†Yanping Yang, Lingfeng Gao and Junxiu Xi contributed equally to this work.

*Correspondence:
Qianfa Long
lonva@live.cn
[1]Department of Neurosurgery, Xi'an Central Hospital, Xi'an Jiaotong University, No. 161, West 5th Road, Xincheng District, Xi'an 710003, P.R. China
[2]College of Medicine, Yan'an University, Yongxiang Road, Baota District, Yan'an 716000, China
[3]Department of Nuclear Medicine, Xi'an Central Hospital, Xi'an Jiaotong University, No. 161, West 5th Road, Xincheng District, Xi'an 710003, P.R. China
[4]Department of Radiology, Xi'an Central Hospital, Xi'an Jiaotong University, No. 161, West 5th Road, Xincheng District, Xi'an 710003, P.R. China

Introduction

Intracerebral hemorrhage (ICH) is a devastating form of stroke characterized by bleeding within the brain parenchyma, accounts 10 ~ 15% of all stroke cases globally [1, 2]. Despite advancements in medical and surgical treatments, mortality rates associated with ICH remain high, with approximately 40% of patients dying within the first month following the hemorrhagic event and only 20% achieving functional independence within six months [1, 3]. The pathophysiology of ICH is complex and multifactorial, involving initial mechanical damage due to hematoma formation, followed by secondary injury resulting from hematoma expansion, inflammation, oxidative stress, and apoptosis [4]. Notably, ferroptosis has been implicated in the progression of neuronal damage following ICH, and therapeutic strategies targeting the modulation of neuronal ferroptosis have gained attention [5–7].

Extracellular vesicles (EVs), including exosomes, are nanosized particles that carry a multitude of bioactive molecules, such as proteins, lipids, and nucleic acids. These are increasingly for their potential as therapeutic targets, biomarkers, innovative drug delivery agents, and standalone treatments [8, 9]. Mesenchymal stem cells (MSCs) and their secretory products, particularly small EVs, have demonstrated considerable promise in the treatment of neurological disorders due to their neuroprotective effects, immunomodulatory capabilities, and the ability to permeate the blood-brain barrier (BBB) [10, 11]. In the realm of ICH therapy, MSCs and their secreted EVs have attracted considerable interest in the scientific community [12], the mechanisms underlying their therapeutic potential include anti-inflammatory effects, neuroprotection and neurogenesis, angiogenesis, as well as the modulation of various cell signaling pathways [13–16]. However, there are still worthwhile areas within this field that warrant further investigation. The importance of EV-microRNAs (miRNAs) transfer is well established in the context of neurodegenerative diseases [17–19]. Notably, MSC-EVs carry various types of miRNAs, which are small non-coding RNAs capable of regulating gene expression [10, 20]. These miRNAs can be transferred to recipient cells, influencing a range of physiological and pathological processes in neurological disorders, making them a compelling therapeutic candidate for ICH.

Herein, we explored the use of MSC-EVs as therapeutic agents for the treatment of ICH, investigating their impact on neuronal damage and potential mechanisms of EV therapy both in vitro and in vivo. Intriguingly, through RNA sequencing (RNA-Seq) in a mouse model, we demonstrated that the neuronal system and metal ion transport were involved in the animal models treated by MSC-EVs, and EV-therapy mitigated neuronal ferroptosis induced by ICH. Furthermore, combined with the miRNA microarray analysis and miRNA modification, our findings showed that the MSC-EVs containing miR-214-3P play a significant role in alleviating neuronal ferroptosis in cell model. This research uncovers a novel and effective therapeutic strategy involving MSC-EVs that can potentially halt the progression of ICH-induced neuronal damage *via* regulating ferroptosis.

Methods

MSC-EVs preparation

Human umbilical cord tissue was obtained from five healthy full-term mothers after informed consent. All procedures were approved by the Ethics Committee of Xi'an Central Hospital, Xi'an Jiaotong University (Approved project: Extracellular Vesicle Biorepository, Approval No. LAS-L-2022-004-01, Date of approval: Mar 21, 2022), and complied with the standards of the National Health Research Institute. MSCs were obtained from Wharton's jelly in the umbilical cord and cultured with αMEM (Hyclone, USA) containing 10% fetal bovine serum (FBS) (Gibico, USA) at 37℃ in 5% CO_2. Flow cytometry analysis was performed using rabbit polyclonal antibodies CD105, CD90, CD45, and CD34 (diluted 1:100; BD Biosciences, USA) to detect the surface antigens of MSCs. Cells from the third passage (P3) were used, adhering to the minimum criteria established by the Mesenchymal and Tissue Stem Cell Committee of International Society for Cellular Therapy [21]. At least three cell culture samples were tested on a flow cytometer (Becton Dickinson, USA) and data were analyzed using Cell Quest software (Becton Dickinson, USA). Cell viability was assessed using the trypan blue exclusion method and quantified with an Automated Cell Counter (BodBoge, JSY-SC-031, China). Only cells with a viability rate exceeding 98% were utilized in subsequent studies.

P3 ~ 5 MSCs were cultured in αMEM containing 10% EV-free FBS, the cell supernatant was collected, and EVs were isolated using differential centrifugation (300 × g for 10 min, 2,000 × g for 10 min, and 10,000 × g for 30 min; ST16R, Thermo Fisher, USA). Subsequently, the supernatant was centrifuged at 100,000 × g (XPN-100, Beckman Coulter, USA) for 60 min to collect the EVs pellet, which was resuspended in sterile phosphate buffer saline (PBS) and centrifuged at 120,000 g (XPN-100, Beckman Coulter, USA) for 70 min to deplete free protein and impurities. The EVs were then stored at -80 °C until use. The protein content of the EV suspension was quantified using a bicinchoninic acid (BCA) assay (Beyotime, P0010, Beijing, China) according to the manufacturer's instructions. The positive markers of EVs, CD9 (1:1000; ab236630, Abcam, USA), TSG101 (1:1000; ab125011, Abcam, USA), and the negative marker calnexin (1:1000; ab22595, Abcam, USA) were determined by Western blotting. The morphology and size distribution of

EVs were detected by transmission electron microscopy (TEM) and nanoparticle tracking analysis (NTA), respectively.

Cell model preparation and administration

HT22 cells (a classic neuronal cell line [22]) were purchased from the Cell Bank of Type Culture Collection of the Chinese Academy of Sciences (Shanghai, China) and maintained in Dulbecco's modified Eagle medium (Invitrogen, CA, USA) supplemented with 10% fetal bovine serum (FBS) (Invitrogen, CA, USA) in a 5% CO_2 incubator at 37 ℃. For the ICH cell model preparation, the neuronal cells were cultured at a density of 5×10^4 in a 96-well plate and treated with PBS, and Hemin (51280, Sigma Aldrich, CA, USA) at concentrations of 10 μmol/L, 20 μmol/L, 40 μmol/L, 60 μmol/L, 80 μmol/L, and 100 μmol/L for 2, 4, 6, 8, 10, 12, and 24 h respectively ($n=6$ samples per group). Hemin was dissolved using 0.1 M NaOH according to the manufacturer's instructions. The culture medium was removed and washed three times with PBS, then 10 μl of CCK-8 (Beyotime, Beijing, China) solution mixed with 100 μL of DMEM was added to each well and incubated for 2 h. The optical density (OD) of neurons at 450 nm was measured using an enzyme-linked immunosorbent assay (ELISA) (Bio-Rad Laboratories Inc., Hercules, CA, USA) to estimate cell viability. Finally, the cell model was prepared by using 80 μmol/L Hemin stimulation for 6 h (Figure S1A), followed by the addition of PBS and MSC-EVs according to the dose responses of MSC-EVs on Hemin-stimulated neurons (Figure S1B).

ICH induction and treatments

Adult male C57BL/6 mice (8～10-weeks old, 25～30 g weight) were purchased from the Experimental Animal Center of Xi'an Jiaotong University. They were housed in groups and were allowed a period to acclimatize to the laboratory environment. All animal procedures were performed in accordance with the ARRIVE guidelines and approved by the Ethics Review Board of Xi'an Central Hospital, Xi'an Jiaotong University (Approved project: Ethical Approval Document for Biological Research, Approval No. 2021－1104, Date of approval: Feb 20, 2021). Animals were housed under a controlled environment with a 12 / 12 h light / dark cycle and provided with food and water. To create the animal model, mice were anesthetized by 2% isoflurane/air mixture inhalation and placed on a stereotaxic instrument. Buprenorphine (0.05 mg/kg) was administered subcutaneously 30 min before surgery for effective analgesia. Autologous blood (25 μl) was injected into the striatum (coordinates: 0.8 mm anterior, 3.0 mm ventral, and 2.0 mm lateral to the bregma) at a rate of 2 μL/min using a Hamilton syringe, according to previous reports [5, 23]. Carprofen (5 mg/kg) was administered immediately post-surgery and daily for three days to manage pain and inflammation. These models were verified by the damage molecular pattern high mobility group protein 1 (HMGB1) expression (Figure S2A) and MRI alterations (Figure S3A and B). ICH mice received 50 μg MSC-EVs (diluted with 150 μL) or same volume of saline via tail vein injection as the ICH+EVs ($n=45$) or ICH+Veh ($n=40$) group, sham-operated mice received the same procedures (e.g., isoflurane anesthesia and needle insertion) or addition of 50 μg MSC-EVs infusion (via tail vein) as the Sham ($n=20$) or Sham+EVs ($n=5$) group. Normal mice were assigned to the Naïve ($n=5$) group. The dose of MSC-EVs administration was determined based on variations in HMGB1 levels (Figure S2B). Additionally, 20 mice were employed to verify the ICH model and test the EVs dose responses. Mice appeared healthy and exhibited normal activity levels prior to the start of the study. Mice exhibiting signs of illness or abnormal behavior were excluded from the study initially. Animals were excluded from analysis only if they experienced complications unrelated to the ICH model or experimental procedures, such as infections or physical abnormalities unrelated to the induced ICH. All the animal experiments mentioned above utilized block randomization to allocate mice to the control and treatment groups.

MSC-EVs tracking in the ICH mice

For tracking the MSC-EVs in vivo, the vesicles were labeled by first shaking them with 0.01% Tin (II) chloride dihydrate for 5 min, then adding ^{99m}Tc (Guangdong CI Medicine Co. Ltd., China) (148MBq ^{99m}Tc / 100 μg MSC-EVs), and shaking for another 30 min as previously described [24]. Labeling efficiency was assessed using instant thin-layer chromatography (TLC), and radioactivity was measured with a Scan-RAM MCA scanner (Lablogic Systems, USA). Stability of the labeled MSC-EVs was tested in PBS with 20% FBS at 37 °C, checking purity at 0- and 3-hours post-incubation. The ICH and Sham mice ($n=3$, per group) were administered with 74 MBq of 99mTc-MSC-EVs *via* tail vein injection. During the imaging process, the mice were anesthetized with 2% isoflurane/air mixture inhalation and kept warm. Gamma camera (Mediso nanoScan SPECT/CT scanner, Hungary) imaging was performed at 3, 6, and 24 h after administration. For tracking the MSC-EVs in vitro, the vesicles were labeled with the C5 Maleimide-Alexa 594 (A954; Invitrogen, A10256, California, USA) as our previous report [25]. The ICH mice were received 50 μg A954-labelled MSC-EVs ($n=3$) or MSC-EVs ($n=3$) infusion *via* tail vein. Brain tissues were collected from the ICH model at 24 h post-injection and processed for immunostaining.

MRI scanning

T1-weighted imaging (T1WI), T2-weighted imaging (T2WI), and Diffusion-Weighted Imaging (DWI) sequences were performed to detect the Sham, ICH+Veh, and ICH+EVs (n=3, per group) with a 3.0-Tesla MR scanner (Philips Ingenia, Netherlands) at 24 h, 3 days, 15 days, and 30 days after MSC-EVs treatment, respectively. Prior to the MRI scan, each mouse in the experimental groups was anesthetized using a 2% isoflurane/air mixture throughout the examination, ensuring they remained still for accurate imaging and reducing stress. A detuned 12-mm surface coil was placed over the skull and centered over the midline of the brain, and the imaging sequences were conducted with the parameters (field of view: 1.8×1.8 cm, spatial resolution: 256×128, reconstruction matrix: 320×320, repetition time: 3000ms, effective echo time: 75ms). The images were preserved as 288×288-pixel pictures for brain swelling analysis, and the alterations were objectively evaluated by at least 3 senior radiologists from Xi'an Central Hospital, Xi'an Jiaotong University. After the MRI scan, the mice were removed from the coil and allowed to recover from anesthesia under close monitoring.

RNA sequencing

To assess the variations in gene expression among the Sham (n=4), ICH+Veh (n=5), and ICH+EVs (n=5) groups after 4 days of EV therapy, total RNA was extracted from the right cortical tissue of each mouse using RNAiso Plus Total RNA extraction reagent (9109, Takara, Japan). RNA integrity was assessed using the RNA Nano 6000 Assay Kit of the Bioanalyzer 2100 system (Agilent Technologies, CA, USA). Briefly, mRNA was purified from total RNA (1 μg) using poly-T oligo-attached magnetic beads. First-strand cDNA was synthesized using random hexamer primer and M-MuLV Reverse Transcriptase. Second-strand cDNA synthesis was subsequently performed using DNA Polymerase I and RNase H. The remaining overhangs were converted into blunt ends by exonuclease/polymerase activities. To select cDNA fragments of preferentially 370～420 bp in length, the library fragments were purified using AMPure XP system (Beckman Coulter, Beverly, USA). Then, PCR was performed with Phusion High-Fidelity DNA polymerase, Universal PCR primers and Index (X) Primer. Finally, PCR products were purified using AMPure XP system and library quality was assessed using Agilent Bioanalyzer 2100 system. The clustering of the index-coded samples was performed on a cBot Cluster Generation System using the TruSeq PE Cluster Kit v3-cBot-HS (Illumina, CA, USA) according to the manufacturer's instructions. After cluster generation, the library preparations were sequenced on an Illumina Novaseq platform and 150 bp paired-end reads were generated (H101SC21010217, Novogene, China). All downstream analyses were based on the clean data with high quality. The index of the reference genome was built and paired-end clean reads were aligned to the reference genome using Hisat2 v2.0.5. Differential expression analysis was performed using the edgeR package (3.22.5). The P-values were adjusted using the Benjamini & 2 Hochberg method and a corrected P-value of 0.05 and absolute fold change of 2 were set as the threshold for significantly differential expression. Gene Ontology (GO), Reactome, and Gene Set Enrichment Analysis (GSEA) of differentially expressed genes were implemented by the clusterProfiler R package, in which gene length bias was corrected.

Transmission electron microscopy

The ipsilateral cortical tissue of ICH mice (n=4, day 4) was fixed in a solution of 2.5% glutaraldehyde and 2% paraformaldehyde (PFA) in 0.1 M cacodylate buffer to preserve ultrastructural details. After fixation, the samples were washed in cacodylate buffer and then post-fixed in 1% osmium tetroxide to enhance contrast. The samples were then dehydrated through a graded series of ethanol solutions, followed by infiltration with a propylene oxide-resin mixture and embedding in pure resin. The resin was polymerized at 60 °C for 48 h to harden. Ultra-thin Sects. (60–90 nm) were cut using an ultramicrotome, mounted on copper grids, and stained with uranyl acetate and lead citrate to enhance contrast. The prepared samples were then examined under a transmission electron microscope (Hitachi TEM system, Japan).

MiRNA microarray for the EVs contained miRNAs

Total RNA from MSC-EVs (n=3) was extracted and purified using the mirVana™ miRNA Isolation Kit without phenol (AM1561, Ambion, TX, USA). Human miRNA microarrays from Agilent Technologies (8×60 K), containing probes for 2549 human miRNAs from the miRbase V21.0 database, were adopted. Total RNA (100 ng) extracted from each EV sample was used as inputs for sample labeling and hybridization preparation in accordance with the manufacturer's protocol (Agilent Technologies, Santa Clara, CA). The miRNA microarray image information was converted into spot intensity values using Scanner Control Software Rev. 7.0 (Agilent Technologies, Santa Clara, CA). Raw data were normalized by a Quantile algorithm, included in the R package AgiMicroRna [26]. Target gene prediction was performed using Target Scan Human 7.2. The miRNA microarray experiments were performed following the protocol of Agilent Technologies Inc at Shanghai Biotechnology Corporation (BC200088, SHBIO, China).

MiRNA transfection and treatment

Modifications to miRNA were carried out using the miR-214-3p inhibitor, mimic, and negative control (NC); the miR-760 inhibitor, mimic, and NC; and U6 as the reference gene, all of which were designed and synthesized by GenePharma (Shanghai, China). The specific sequences for these modifications are provided in Table S8. HT22 cells were pre-treated with 10 μg of MSC-EVs, following the protocol described previously [17]. Subsequently, the neurons underwent miRNA interference (Figure S4) using the Lipofectamine 3000 kit (L3000001, Thermo Fisher Scientific, USA), as per the manufacturer's guidelines, coupled with Hemin stimulation. The cellular experimental cohorts were then categorized as follows: the HT22-only group (HT22), the ICH cell model interfered with NC group (HT22-Hemin+NC), the ICH cell model group treated with miRNA mimics (HT22-Hemin+miR-214-3p/miR-760 mimics), and the ICH cell model group treated with miRNA inhibitors alongside MSC-EVs (HT22-Hemin+EVs+miR-214-3p/miR-760 inhibitor). Additionally, quantitative Real-time PCR was employed to measure the mean expression levels (2-ΔΔCt) of the miRNAs in the cell models, with three replicates per group.

Immunofluorescence staining

The animals (n=5, per group) were sacrificed with isoflurane and perfused intracardially with cold 4% PFA solution on day 4. After that, the brain sections were selected and processed for histological study as previously described [17, 27]. The neuronal cell samples (n=6, per group) were fixed with 4% PFA and stored in a -20 °C freezer. Before staining, the cell or tissue samples were washed three times with PBS, then treated with PBS solution containing 0.1% Triton-X 100 and 10% goat serum for 30 min. They were then incubated overnight at 4 °C with the NeuN (1:1000; ABN78, Millipore, USA), GPX4 (1:500; ab125066, Abcam, USA), HMGB1 (1:250; ab228624, Abcam, USA), HSP70 (1:400; ab181606, Abcam, USA), or 8-OHDG (1:200; AB5830, Millipore, USA) primary antibodies. The next day, after washing with PBS, the samples were incubated with the corresponding secondary antibodies for 2 h and the cell nuclei were detected with 4',6-diamidino-2-phenylindole (DAPI; D9542, Sigma-Aldrich, CA, USA). The Mito-FerroGreen kit (M489, Dojindo, Japan) was also used to detect the cell samples according to the manufacturer's instructions. Images were taken using a FV3000 confocal microscope (Olympus, Japan) and analyzed using ImageJ Pro Plus V 6.0 (Bethesda, Maryland, USA).

Western blotting

Proteins were extracted from the cell and animal models (ipsilateral cortical samples) in each group (n=5 per group) using Radio-Immunoprecipitation Assay (RIPA) lysis buffer (P0013B, Beyotime, Beijing, China) and quantified using a BCA kit. The protein samples were all normalized to the same concentration, and the normalized protein samples were subjected to sodium dodecyl sulfate-polyacrylamide gel electrophoresis (SDS-PAGE), and then transferred to a polyvinylidene fluoride membrane (Millipore, MA, USA). The membranes were blocked at room temperature for 1 h with a BSA (Solarbio, Beijing, China) blocking solution, and then incubated overnight at 4 °C with primary antibodies against Nrf2 (1:1000; 16396-1-AP, Proteintech, USA), HO-1(1:1000; 10701-1-AP, Proteintech, USA), HMGB1 (1:1000), NOX2 (1:1000; MA5-18051, Thermo Fisher, USA), ACSL4 (1:1000; 9189, CST, USA), GPX4 (1:2000), HSP70 (1:1000), and β-actin (1:20,000; 81115-1-RR, Proteintech, USA), followed by three washes with TBST. The membranes were then incubated at room temperature for 2 h with horseradish peroxidase-conjugated secondary antibodies (1:5000; Proteintech, USA). The labeled proteins were detected using a Bio-Rad imaging system (Bio-Rad, Hercules, CA, USA), and quantification was based on the expression of β-actin protein using Image Lab software (Bio-Rad, Hercules, CA, USA).

Real time quantitative PCR (qPCR)

qPCR was performed to assess the miRNAs and gene expression in the experimental groups. Total RNA was extracted from the cell samples (n=4–5 per group) using the TRIzol reagent (15596026, Life Technologies, USA) according to the manufacturer's protocol. All primer sequences (Table S8) were designed and optimized by TaKaRa (TaKaRa, Dalian, China) including GPX4, ACSL4, GAPDH, mmu-miR-214-3p, mmu-miR-760, common-R, and Mus-U6. The concentration and purity of RNA were assessed using a NanoDrop ND-1000 spectrophotometer (ThermoFisher Scientific, Waltham, USA). Complementary DNA (cDNA) was synthesized from 1 μg of total RNA using the High-Capacity cDNA Reverse Transcription Kit (4368813, ThermoFisher Scientific, USA). qPCR was performed using the TB Green Premix Ex Taq II (RR820A, Takara, Japan) on a CFX Connect real-time PCR detection system (Bio-Rad, CA, USA). Relative gene expression levels were calculated using the 2^-ΔΔCT method, with GAPDH or Mus-U6 serving as the internal control. All reactions were performed in triplicate and the data were analyzed using Bio-Rad CFX Manager 2.1.

Statistical analysis

All observers were blinded to the experimental group assignment and data were examined by the Kolmogorov-Smirnov (K-S) test to determine distribution ($P \geq 0.05$ was employed in the following analysis). Data are presented

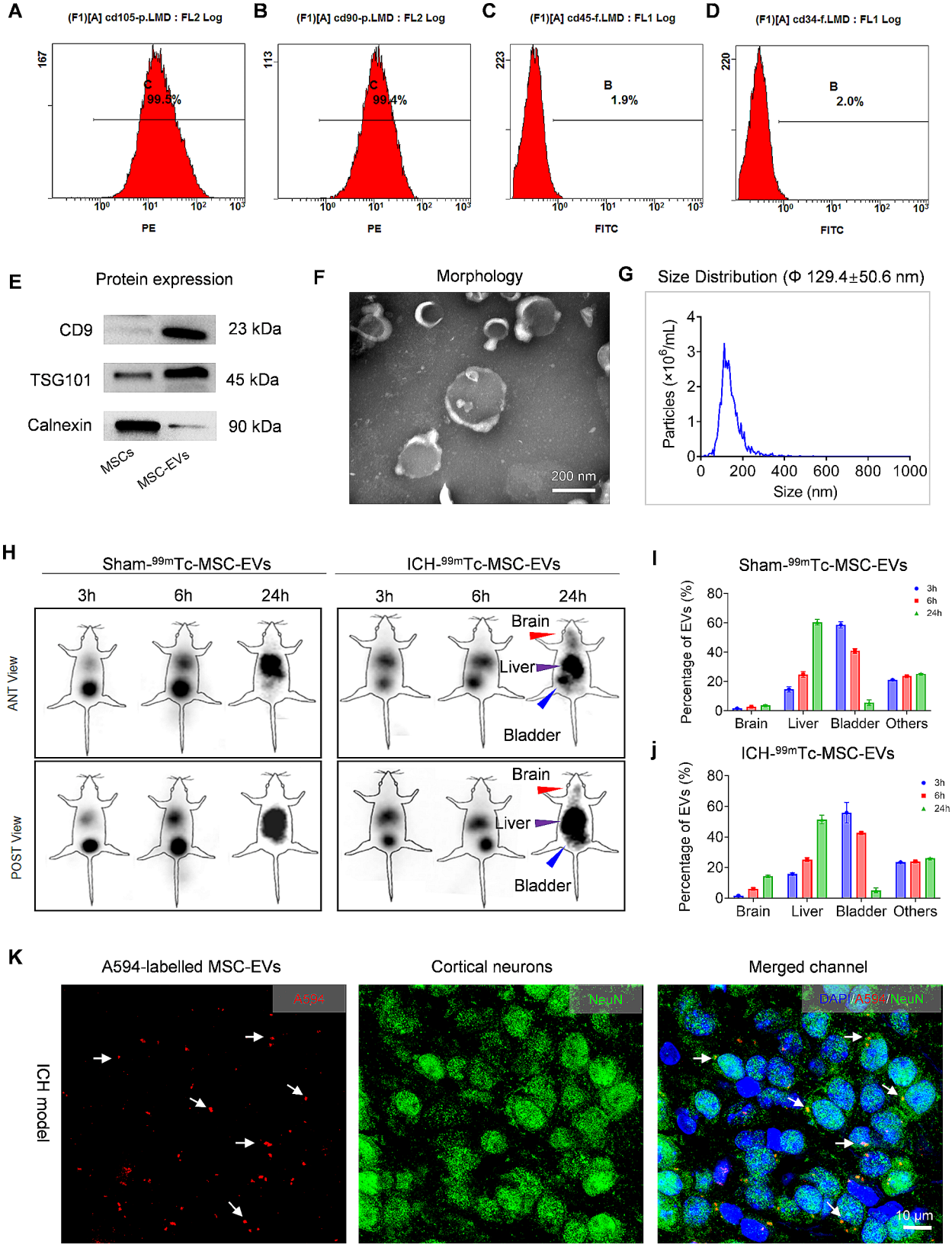

Fig. 1 (See legend on next page.)

(See figure on previous page.)

Fig. 1 MSCs/EVs characterization and EVs tracking.Flow cytometry analysis confirms the presence of mesenchymal (**A-C**) and hematopoietic (**D**) markers, including CD105 (**A**), CD90 (**B**), CD45 (**C**), and CD34 (**D**) in mesenchymal stem cells (MSCs), respectively. (**E**) Western blots show the vesicular markers CD9, TSG101, and the absence of the endoplasmic reticulum marker calnexin in MSCs-derived extracellular vesicles (MSC-EVs) compared to the control (MSCs). (**F**) The ultrastructure of MSC-EVs is depicted by transmission electron microscopy (TEM), showcasing the characteristic "cup-shaped" morphology. (**G**) Nanoparticle tracking analysis (NTA) illustrates the size distribution of the MSC-EVs. (**H**) Gamma camera imaging shows the localization and concentration of 99mTc -labelled MSC-EVs within both the sham-operated mice (left panel) and the intracerebral hemorrhage (ICH) mice (right panel), with the animals positioned supine (Anterior (ANT) views display the dorsal side, while posterior (POST) views show the ventral side), captured at various time intervals. (**I and J**) Data analysis shows the percentage of EVs uptaken by brain, liver, bladder and others in sham (**I**) and ICH (**J**) mice. (**K**) Representative fluorescence microscopy images demonstrate the uptake of Alexa 594-labeled vesicles (red) by cortical neurons (green) in the ICH model, white arrows show the location of the infused MSC-EVs (red). Scale bar = 10 μm

as mean±standard error of the mean (SEM). One-way analysis of variance (ANOVA) and least significant difference (LSD) tests were used for multiple comparisons with Bonferroni post hoc test conducted using SPSS 26.0.0 and GraphPad Prism 9 software (Graphpad Prism, USA). A *P* value of less than 0.05 was considered statistically significant.

Above work has been reported in line with the ARRIVE guidelines 2.0.

Results

MSCs-EVs characterization and tracking

Flow cytometry was used to examine the surface antigens of MSCs as previous reports [17, 21]. The analysis revealed a high expression of stromal markers CD105 (99.5%) and CD90 (99.4%), and a low expression of hematopoietic markers CD45 (1.9%) and CD34 (2.0%) in these cells (Fig. 1A-D). Further validation of the multipotency of MSCs demonstrated their ability to differentiate into osteoblasts, chondroblasts, and adipocytes. Characterization of EVs derived from MSCs showed that the vesicles exhibited a strong expression of membrane protein CD 9 and TSG101, while calnexin was expressed at lower levels compared to their parent cells (Fig. 1E). Transmission electron microscopy (TEM) and Nanoparticle Tracking Analysis (NTA) revealed that the MSC-EVs display a typical cup-shaped morphology (Fig. 1F) and have an average diameter of 129.4±50.6 nm (Fig. 1G). These characteristics align with the established criteria for EVs as per the guidelines of the International Society for Extracellular Vesicles [28].

After the MSC-EVs were efficiently labeled with ^{99m}Tc (labeling efficiency: 98±0.2%; Figure S5), both the ICH model and Sham mice received 50 μg 99mTc-labeled MSC-EVs (Figure S2B) injection *via* tail vein, followed by imaging with a nanoScan SPECT/CT (Mediso, Hungary). At 3- and 6-hours post-injection, we noted a pronounced accumulation of ^{99m}Tc-MSC-EVs in the liver and bladder of both the ICH and Sham mice (Fig. 1H). Even though a substantial proportion of the 99mTc-MSC-EVs still distributed in the liver and bladder of the experimental groups (ICH and Sham) at 24 h after treatment, a distinct uptake of ^{99m}Tc-MSC-EVs in the brain was evident in the ICH model (14.39±0.64%, Fig. 1i) compared to the Sham group (3.67±0.47%, Fig. 1j), indicating the tropism of infused MSC-EVs towards damaged brain in the ICH mice. Moreover, subsequent to 24 h post-injection with A594-labeled MSC-EVs (red), immunostaining revealed that the NeuN-positive nuclei (green) are closely associated with numerous red vesicles in the ipsilateral cortex of the ICH model (Fig. 1k), suggesting that the administered MSC-EVs can target ICH-insulted cortical neurons.

EVs administration ameliorates magnetic resonance imaging (MRI) alterations in ICH mice

After creation of the ICH models, the Sham, ICH+Veh, and ICH+EVs mice were conducted with MRI scanning (Figure S3A), the T2-weighted imaging (T2WI) was finally used to scan the ICH models because the sequence is highly sensitive to deoxyhemoglobin [29]. As it's shown in Figure S3B, T2WI provided the better distinct imaging of the brain parenchyma in sham mice. After EVs treatment for 24 h, the axial segmentation-based T2WI images did not show apparent differences between the ICH+Veh and ICH+EVs group in the hemorrhagic lesion (hypointense) and perihemorrhagic region (Figure S3C). MRI scans conducted on the recipient mice after 3 days showed that the lesions in the vehicle control contained regions with mixed hypointense and hyperintense, while the EVs treated mice primarily displayed hyperintense (Figure S3D). Moreover, the ICH+Veh group exhibited more pronounced signs of vasogenic edema than the ICH+EVs group in the ipsilateral cerebral cortex (Figure S3D). Following the administration of MSC-EVs for 15 days, the images showed that most of the hemorrhagic foci were absorbed in both the vehicle and experimental group (Figure S3E). However, compared to the ICH+Veh group, the ICH+EVs group presented a clearer and more uniform image (Figure S3E). At 30 days post-treatment, T2WI screening of the recipient mice showed substantial absorption of the hemorrhagic foci, and the ipsilateral cerebral cortex displayed normal signals in both the vehicle control and EV-treated group (Figure S3F). Totally, the MRI assessments implied that injection of MSC-EVs improves the ipsilateral imaging resulted by ICH during the subacute stage.

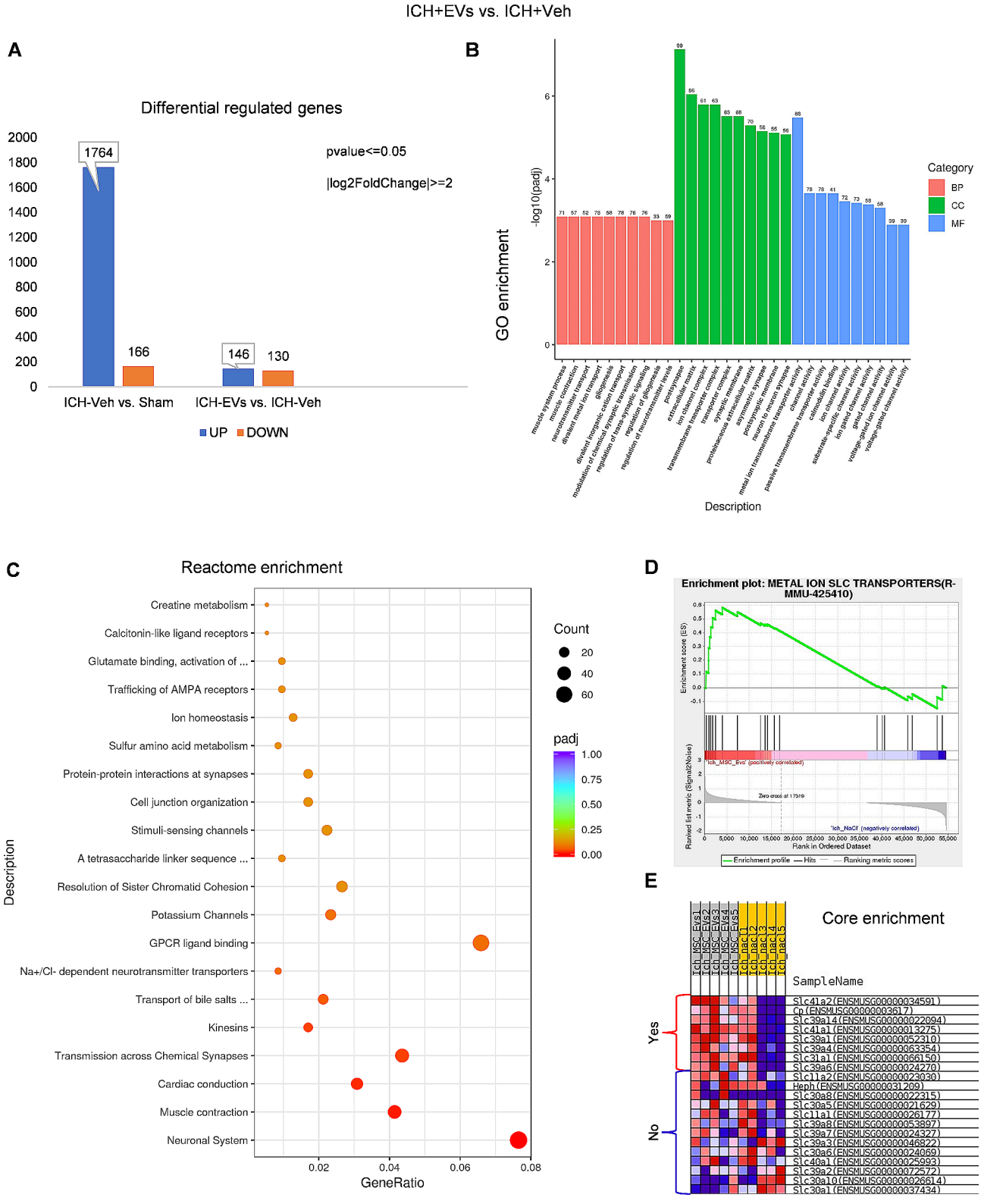

Fig. 2 (See legend on next page.)

(See figure on previous page.)

Fig. 2 RNA-Seq analysis of the ICH model following EV treatment.(**A**) The histogram displays the count of differentially regulated genes when comparing the vehicle control group (ICH-Veh) to the Sham group, as well as the comparison between ICH-EVs and ICH-Veh group. (**B**) Gene Ontology (**GO**) enrichment analysis for the differentially expressed genes, categorized into biological processes (**BP**), cellular components (**CC**), and molecular functions (**MF**), highlights the distinct biological themes modulated by EV therapy in the ICH + EVs group compared to the vehicle control. (**C**) The Reactome pathway enrichment bubble chart highlights the top 20 signaling pathways of the ICH + EVs group compared to the vehicle control, with pathways relevant to the neuronal system emphasized with a blue dashed box. (**D**) Gene Set Enrichment Analysis (**GSEA**) reveals the significant association of the metal ion solute carriers (**SLC**) transporters pathway (R-MMU-425410) in the ICH + EVs group relative to the vehicle control, indicating a potential mechanistic pathway influenced by EV therapy. (**E**) The core enrichment of specific SLC transporter genes, including Slc41a2, Ceruloplasmin (**Cp**), Slc39a14, Slc41a1, Slc39a1, Slc39a4, Slc31a1, and Slc39a6, underscores the targeted impact of EV therapy on metal ion homeostasis post-ICH

RNA-Seq indicates the involvement of neuronal system and metal ion transport in ICH mice following EVs injection

To explore the therapeutic mechanism of MSC-EVs on ICH-resulted ipsilateral cortical injury, transcriptional group sequencing was performed to evaluate variations in gene expression among the sham, ICH + Veh, and ICH + EVs groups on day 4. Differential gene expression was analyzed by edgeR according to the fragments per kilobase of exon model per million mapped reads (FPKM) (Figure S6A), which were selected for detailed functional genomics based on Log2 fold change (FC) ≥ 2 or ≤ −2, and *P* value ≤ 0.05 (Fig. 2A; Figure S6B). Compared with the sham group, mice in the ICH + Veh group presented 1764 upregulated mRNAs and 166 downregulated mRNAs (Figure S6B, Table S1). A total of 146 upregulated mRNAs and 130 downregulated mRNAs (Table S2) were selected between the ICH + EVs and ICH + Veh groups. Notably, a series of genes associated with neuronal restoration were typified by the upregulated neurotrophic tyrosine kinase receptor type 1 (Ntrk1) [30], thyrotropin-releasing hormone (Trh) [31], and downregulated NADPH oxidase 1 (Nox1) [32], Interleukin 25 (IL-25), etc. (Table S2). Gene Ontology (GO)-based functional enrichment analysis of differentially expressed genes related to biological processes (BP), cellular components (CC), and molecular functions (MF), compared with the sham group (Figure S6C), BP terms showed many immune responses, such as positive regulation of immune response (GO:0050778), adaptive immune response (GO:0002250), T cell activation (GO:0042110), were enriched in the ICH + Veh group (Figure S6C) as previous report [33]. After EVs administration (ICH + EVs), divalent metal ion transport (GO:0070838) and divalent inorganic cation transport (GO:0072511) were markedly enriched in the BP terms in comparison to ICH + Veh group (Fig. 2B; Table S3). Reactome pathway enrichment analysis revealed that, compared with the sham group, immunomodulatory pathways including Toll-Like Receptors Cascades (R-MMU-168898), Signaling by Rho GTPases (R-MMU-194315), Cytokine Signaling in Immune system (R-MMU-1280215) were enriched in the ICH + Veh group (Figure S6D) as previously studied [33]. Remarkably, Neuronal System (R-MMU-112316) pathway was significantly enriched in ICH + EVs group in comparison to the ICH + Veh group (Fig. 2C; Table S4). GSEA showed that, compared to the ICH + Veh group, metal ion solute carriers (SLC) transporters (R-MMU-425410) pathway was enriched after MSC-EVs treatment (ICH + EVs) (Fig. 2D), as well as typified by the core enrichment of Slc41a2, Ceruloplasmin (Cp), Slc39a14, Slc41a1, Slc39a1, Slc39a4, Slc31a1, and Slc39a6 genes (Fig. 2E). Considering the significance of metal ion transport in the ferroptosis initiation and progression [34], these data suggest that the neuronal ferroptosis are markedly involved in the animal models followed by EVs injection.

EVs infusion alleviates the neuronal damage in ipsilateral cortical areas of ICH mice

Based on the enrichment of neuronal system in the experimental groups, the neuronal restoration was assessed by analyzing the oxidative stress and damage-associated molecular patterns (DAMPs) in ipsilateral cortical areas from each group at 24 h, 4 days, or 30 days using Western blotting and immunoassay. Compared to the ICH model (ICH + Veh), protein analysis (Fig. 3A) revealed a significant increase in the expression of Nrf2 (Fig. 3B) and HO-1 (Fig. 3C) in the ICH + EVs group ($P < 0.001$, at 24 h and 4 days). Conversely, NOX2 expression significantly decreased ($P < 0.0001$) following MSC-EVs treatment at the same time points (Fig. 3D). However, no significant differences were found between the ICH + Veh and ICH + EVs groups on day 30 (Fig. 3B-D). Also, the ICH-induced upregulation of DAMPs (HMGB1 and HSP70) in the ICH + Veh group (Fig. 3E and F) was notably reduced ($P < 0.01$) by EVs administration (ICH + EVs) on day 4 (Fig. 3E and F). Interestingly, compared to the Sham group, the HMGB1 expression significantly increased ($P < 0.001$) at 24 h in the ICH + Veh group (Fig. 3E), but was reduced ($P < 0.05$, vs. ICH + Veh) following MSC-EVs treatment (Fig. 3E). To determine whether these changes occurred in the neuronal system of the recipient mice, double immunostaining of NeuN (neuronal marker) with DAMPs (HMGB1/HSP70) and 8-OHdG (oxidative damage marker) was performed on day 4 in the experimental groups (Fig. 3G). Mean Fluorescence Intensity (MFI) analysis showed that HMGB1 (Fig. 3H), HSP70 (Fig. 3I) and 8-OHdG (Fig. 3J) expression significantly increased ($P < 0.01$) in the ICH model (ICH + Veh) compared to the sham group, while a significant decrease ($P < 0.05$, vs. ICH + Veh) in these damage markers (Fig. 3H-J) was

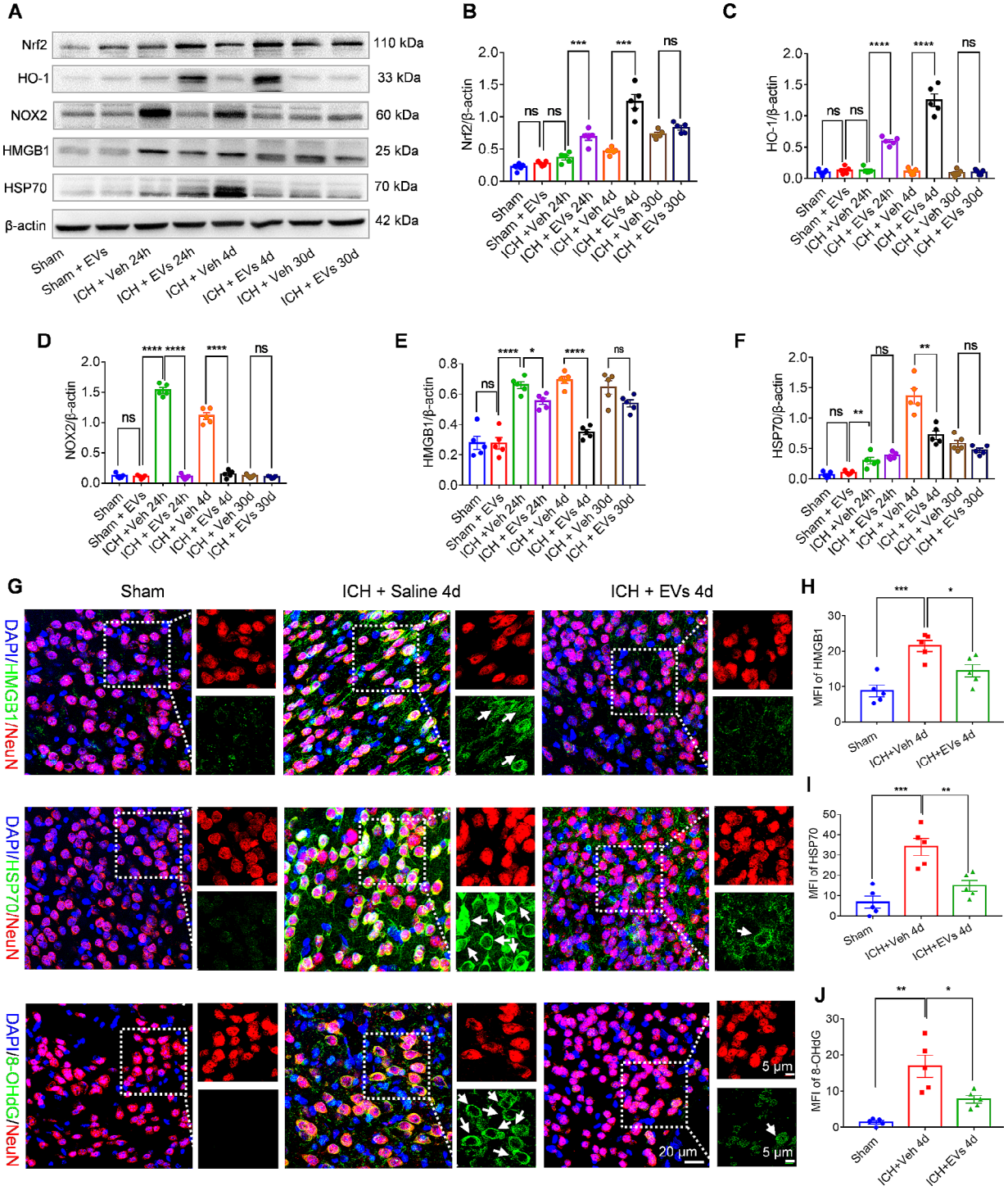

Fig. 3 Therapeutic effects of MSC-EVs on ICH-induced neuronal damage.(**A**) Western blot analysis illustrates the temporal expression patterns of oxidative stress markers and damage-associated molecular patterns (DAMPs) across different groups: Sham, Sham + EVs, ICH + Veh, and ICH + EVs. Full-length blots are presented in Figure S7. (B-F) Quantitative histograms depict the differential expression levels of neuroprotective and oxidative stress-related proteins including Nrf2 (**B**), HO-1 (**C**), NOX2 (**D**), HMGB1 (**E**), and HSP70 (**F**) following treatment with EVs, compared to the control groups. (**G**) Immunostaining demonstrates the localization of neuronal damage markers HMGB1, HSP70, and the oxidative DNA damage marker 8-OHdG (co-stained with the neuronal marker NeuN) in the Sham, ICH + Veh, and ICH + EVs groups at day 4 post-injury. Scale bars: left images, 20 μm; right images, 5 μm. (**H-J**) The mean fluorescence intensity (**MFI**) for HMGB1 (**H**), HSP70 (**I**), and 8-OHdG (**J**) is quantified and presented in corresponding histograms for each experimental group. Data are expressed as mean ± SEM. The normality of distribution was verified using the Kolmogorov-Smirnov (**K–S**) test. Statistical differences between groups were assessed using one-way ANOVA followed by the least significant difference (**LSD**) test for multiple comparisons. Significance levels are indicated as $^{ns}P > 0.05$, $^{*}P < 0.05$, $^{**}P < 0.01$, $^{***}P < 0.001$, $^{****}P < 0.0001$

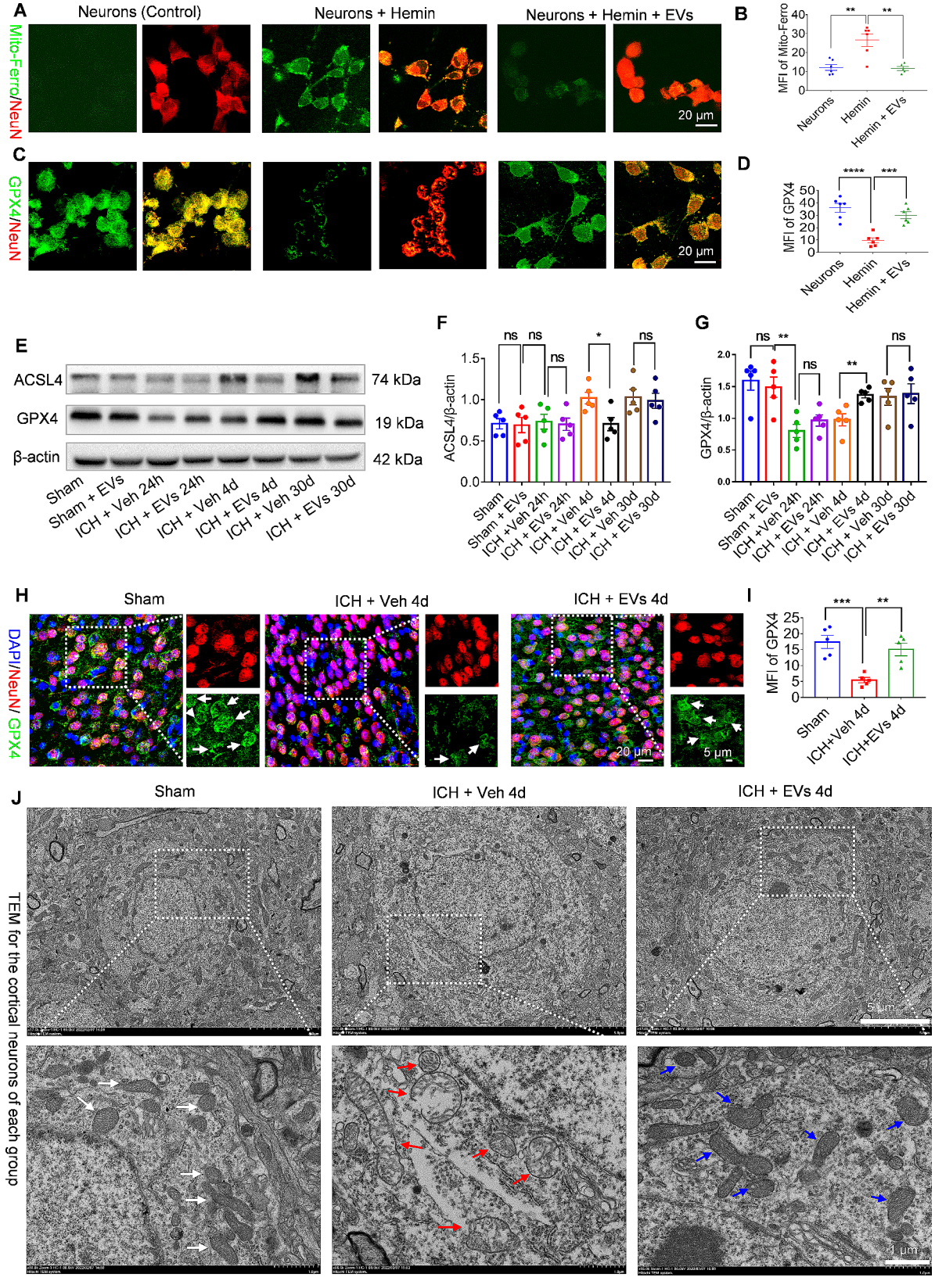

Fig. 4 (See legend on next page.)

(See figure on previous page.)

Fig. 4 EV therapy alleviates neuronal ferroptosis in cell and animal models of ICH.(**A** and **C**) Immunostaining highlights the mitochondrial iron accumulation (Mito-Ferro, green, **A**) and the ferroptosis marker GPX4 (green, **C**) co-localized with the neuronal marker NeuN (red) in hemin-stimulated neuronal cell cultures. Scale bars = 20 μm. (**B** and **D**) The mean fluorescence intensity (MFI) of Mito-Ferro (**B**) and GPX4 (**D**) is quantitatively analyzed and depicted in the corresponding histograms for each experimental group. (E) Western blot analysis reveals the expression levels of ACSL4 (a lipid metabolism-regulating enzyme indicative of ferroptosis) and GPX4 in the experimental groups: Sham, Sham + EVs, ICH + Veh, and ICH + EVs. Full-length blots are presented in Figure S8. (**F-G**) Histograms provide a quantitative comparison of the expression levels of ferroptosis-related proteins ACSL4 (**F**) and GPX4 (**G**) after EV treatment compared to controls. (H and I) Double immunostaining for GPX4 (green) and NeuN (red) in tissue sections (ipsilateral cortical areas) from the experimental groups on day 4 post-ICH, with quantification of GPX4 MFI presented in histograms (**I**). Scale bars for left images, 20 μm; right images, 5 μm. (**J**) Transmission electron microscopy (TEM) images display mitochondrial morphology after EV treatment at day 4 in the experimental groups. The magnified images show mitochondrial swelling, membrane integrity, and cristae structure in the ipsilateral cortical neurons of the Sham (white arrow), ICH + Veh (red arrow), and ICH + EVs (blue arrow) groups. Scale bars for upper images, 5 μm; lower images, 1 μm. Statistical analyses were performed after confirming the normality of data distribution using the Kolmogorov-Smirnov (**K–S**) test. Group differences were evaluated using one-way ANOVA with the least significant difference (**LSD**) test for multiple comparisons. Significance is denoted as $^{ns}P > 0.05$, $^{*}P < 0.05$, $^{**}P < 0.01$, $^{***}P < 0.001$, $^{****}P < 0.0001$

observed following EV therapy (ICH + EVs). Additionally, we did not find any influence of EVs infusion on Sham mice ($P > 0.05$, Fig. 3B-F). Collectively, these results suggest that MSC-EVs administration alleviates the neuronal damage in ipsilateral cortical areas caused by ICH.

MSC-EVs alleviate neuronal ferroptosis in Hemin-stimulated neuronal cells and ICH mice

After Hemin stimulation of neuronal cells (Neurons + Hemin), ferroptosis was characterized by the increased Mito-FerroGreen (iron ion fluorescence probe) (Fig. 4A and B) and decreased GPX4 (ferroptosis marker) (Fig. 4C and D) staining in comparison to the control group. Remarkably, MSC-EVs administration (Neurons + Hemin + EVs) significantly reversed the neuronal changes induced by Hemin. Also, the representive markers (ACSL4 and GPX) of ferroptosis were examined by Western blotting at 24 h, 4 days and 30 days in the ipsilateral cortical tissues of recipient mice (Fig. 4E). Compared to the sham group, ICH (ICH + Veh) resulted in an upregulation ($P < 0.01$) of ACSL4 expression on day 4 and day 30 (Fig. 4F), as well as a downregulation ($P < 0.01$) of GPX4 expression at 24 h and 4 days (Fig. 4G) in the cortical samples. Notably, the significant differences ($P < 0.05$) between ICH + EVs and ICH + Veh for the ACSL4 and GPX4 expression were only shown on day 4 (Fig. 4F and G). We did not find the influence ($P > 0.05$) of MSC-EVs on the Sham group (Sham + EVs vs. Sham). Meanwhile, double immunostaining with GPX and NeuN was further used to illustrate neuronal ferroptosis in the experimental groups (ipsilateral cortical tissues) on day 4 (Fig. 4H). Mean fluorescence intensity (MFI) analysis showed that MSC-EVs therapy (ICH + EVs) significantly increased ($P < 0.01$) the GPX expression induced by ICH (Fig. 4I). Moreover, given that the mitochondrial alterations are a typical change in ferroptosis [35], a transmission electron microscope (TEM) was employed to detect the neuronal alterations in each group (ipsilateral cortical tissues) on day 4. Compared to the sham group, ICH (ICH + Veh) resulted in mitochondrial membrane swelling, outer membrane rupture, and decreased or disappeared mitochondrial ridges, while the administration of MSC-EVs (ICH + EVs) obviously restored the mitochondrial changes induced by ICH (Fig. 4J). Taken together, these results indicate the alleviation of neuronal ferroptosis by MSC-EV treatment in vitro and in vivo.

EV-miR-214-3p inhibits the hemin-induced neuronal ferroptosis

Given the significance of miRNAs in EV-based therapy [36, 37], we utilized miRNA microarray analysis to detect the miRNAs that were enriched in MSC-EVs and investigated the candidates that were involved in the neuronal ferroptosis modulation. After quality control, we showed that 289 miRNAs were expressed in all three MSC-EVs samples (Table S5), and 96.19% of these EV-miRNAs were matched with the Vesiclepedia database (Fig. 5A). Based on the miRNA target (e.g., GPX4, ACSL4) predictions, we selected miR-615-3p, miR-4488, miR-214-3p, miR-199a-3p, miR-199b-3p, miR-34c-5p, miR-34a-5p, and miR-760 as potential regulators of ferroptosis from the top 20 EV-miRNAs (Fig. 5B, Table S6). Kyoto Encyclopedia of Genes and Genomes (KEGG) analysis showed that the target genes of these EV-miRNAs (above 8 selected miRNAs) were enriched in the ferroptosis-associated pathways such as the HIF-1 signaling pathway (hsa04066) [38], Neurotrophin signaling pathway (hsa04722) [22], and AMPK signaling pathway (hsa04152) [39] (Fig. 5C, Table S7). Furthermore, based on their high total scores and low total energy as indicated in EV-miRNAs (Table S6), miR-760 and miR-214-3p mimics / inhibitors were employed to emulate the EV-miRNA modifications for treating Hemin-induced HT22 cells. Quantitative Real-time PCR (qPCR) analysis revealed that miR-760 interference (HT22-Hemin + miR-760 mimics / HT22-Hemin + EVs + miR-760 inhibitor) positively impacted the expression of GPX4, a ferroptosis marker, compared to both the negative control (HT22-Hemin + miR-760 mimics vs. HT22-Hemin + NC; $P < 0.001$) and the EV-treated group (HT22-Hemin + EVs + miR-760 inhibitor vs. HT22-Hemin + EVs; $P < 0.0001$) (Fig. 5D). However, the modification of miRNA in MSC-EVs did not demonstrate a regulatory effect on HMGB1 expression, a marker of neuronal damage, in the ICH cell model (both

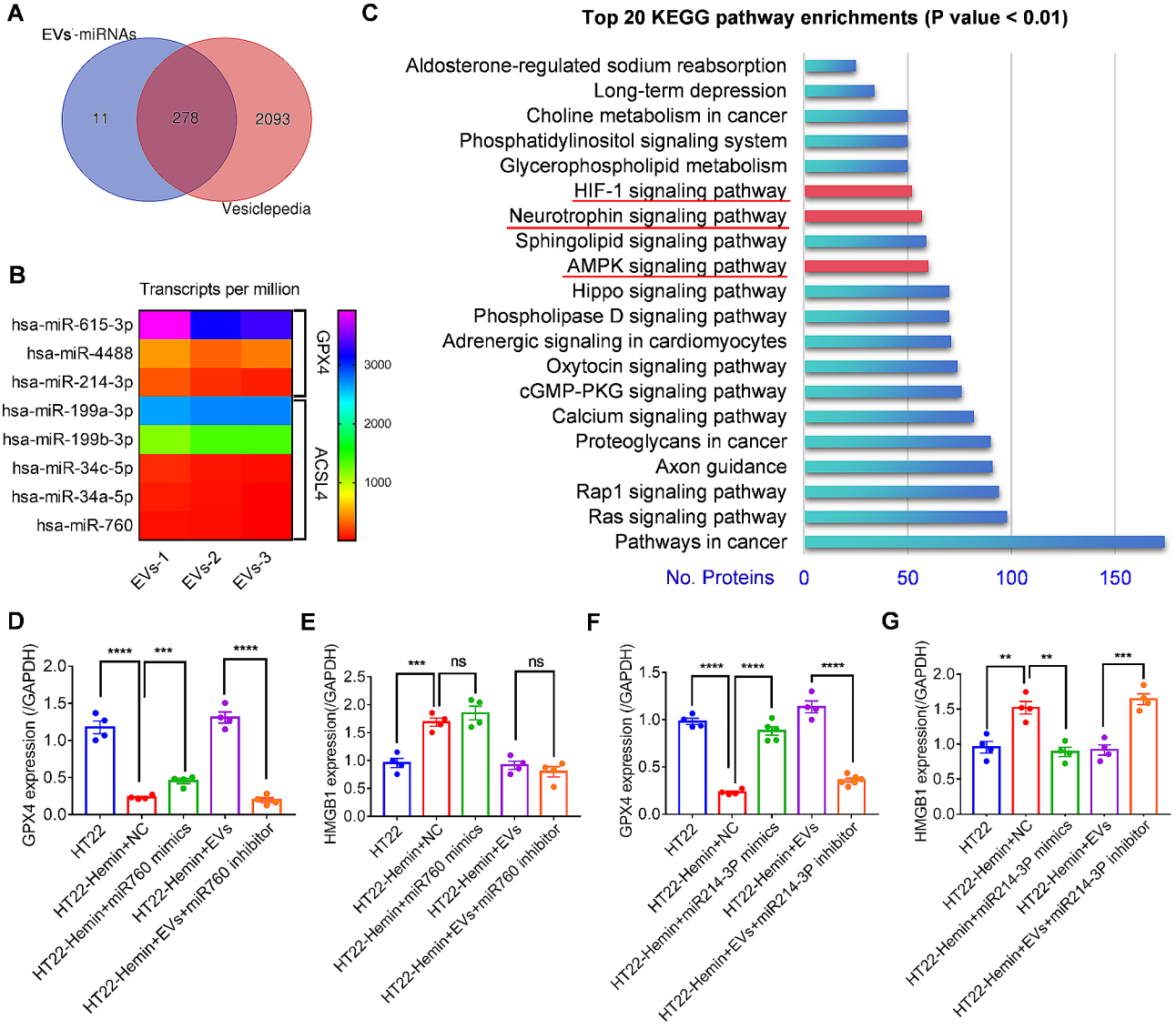

Fig. 5 EV-miRNAs target ferroptosis marker genes and mitigate the ferroptosis-mediated neuronal damage.(**A**) Following miRNA microarray analysis of MSC-EVs, 96.19% of EV-miRNAs (289 in total) were found to correspond with entries in the Vesiclepedia database. (**B**) A heatmap reveals the 8 EV-miRNAs that target the ferroptosis marker genes GPX4 or ACSL4. (**C**) Analysis using the Kyoto Encyclopedia of Genes and Genomes (KEGG) identified the top 20 pathways enriched among the target genes of the selected miRNAs, highlighting ferroptosis-related pathways with red lines. Based on overall scores and energy parameters, miR-760 and miR-214-3p were chosen for further investigation to ascertain the regulatory impact of EV-miRNAs on the ICH cell model. (**D-G**) Subsequent to miRNA interference, qPCR results demonstrated the relative RNA expression levels of GPX4 (a ferroptosis marker) and HMGB1 (a marker of neuronal damage) across the study groups. Group differences were evaluated using one-way ANOVA with the least significant difference (**LSD**) test for multiple comparisons. Significance is denoted as $^{ns}P > 0.05$, $^{*}P < 0.05$, $^{**}P < 0.01$, $^{***}P < 0.001$, $^{****}P < 0.0001$

HT22-Hemin+miR-760 mimics vs. HT22-Hemin+NC and HT22-Hemin+EVs+miR-760 inhibitor vs. HT22-Hemin+EVs; $P > 0.05$) (Fig. 5E). This suggests that while EV-miR-760 may play a role in the regulation of ferroptosis signaling, it does not influence neuronal damage in Hemin-stimulated HT22 cells. Remarkably, treatment with miR-214-3p mimics (HT22-Hemin+miR-214-3p inhibitor) effectively reversed the Hemin-induced downregulation of GPX4 ($P < 0.01$, Fig. 5F) and upregulation of HMGB1 ($P < 0.01$, Fig. 5G) compared to the negative control (HT22-Hemin+NC). Additionally, miR-214-3p inhibitor interference (HT22-Hemin+EVs+miR-214-3p inhibitor) diminished the therapeutic effects of MSC-EVs, as evidenced by decreased GPX4 expression ($P < 0.0001$, Fig. 5F) and increased HMGB1 expression ($P < 0.001$, Fig. 5G) relative to the HT22-Hemin+EVs group. These findings collectively indicate that miR-214-3P, contained within MSC-EVs, plays a pivotal regulatory role in addressing ferroptosis-mediated neuronal damage in the ICH cell model.

Discussion

To our knowledge, this is a novel study that elucidates the ability of MSC-EVs to prevent cortical neurons from damage via regulating ferroptosis in a mouse model of ICH. Ferroptosis is implicated in the initiation and progression of neuronal damage following ICH [6] and considering the neuroprotective and reparative capabilities of MSC-EVs in neurological disorders [10]. Accordingly, we demonstrated that tail-vein injection of MSC-EVs alleviates the ICH-induced imaging alterations and neuronal damage. Moreover, RNA-Seq revealed that neuronal systems and metal ion transport are enriched in the ICH model following MSC-EVs infusion. Notably, we demonstrate that MSC-EVs protect neurons from ferroptosis both in vitro and in vivo, as well as highlight the role of EV-miRNA-214-3p in the regulation of neuronal ferroptosis. Using EVs in our study offers a safer alternative to MSC delivery [40] by mitigating the risk of capillary embolism due to their significantly smaller size, which enhances delivery efficiency and focuses on the cellular and molecular therapeutic effects post-ICH. These results represent a significant advancement and therapeutic mechanism using MSC-EVs in ICH models.

EV therapy is increasingly recognized as a promising approach in treating neurological disorders due to their neuroprotection and immunomodulatory properties [10, 41]. The ability of EVs to cross the blood-brain barrier (BBB) represents a substantial advantage, positioning them as effective nanotherapeutic agents in the central nervous system diseases [42]. Following the infusion of ^{99m}Tc-labelled MSC-EVs in the experiments, their accumulation in the ICH-affected brain indicates that MSC-EVs possess the capacity to traverse the BBB and are inclined to home to the areas of cerebral damage. Considering the enrichment of neuronal systems followed by EVs treatment, we also examined the biodistribution of labeled MSC-EVs in the ICH insulted cortical area, and showed that the cortical neurons are surrounded by the infused vesicles, which may provide a conducive microenvironment for the injected EVs to exert therapeutic effects on the damaged neurons in a mouse model of ICH. ICH results in a series of histological alterations including hemosiderosis, hematoma formation, and inflammation, which can be characterized by certain features on magnetic resonance imaging (MRI) [43, 44]. We thus used MRI to evaluate the imaging alterations between the experimental group and vehicle control. In line with the MRI signal of ICH changes over time [44], MSC-EVs administration apparently restored ICH-induced signal alterations on T2-weighted images on day 3 and 14, suggesting the therapeutic action of MSC-EVs on ICH ipsilateral imaging during the subacute stage. Notably, the changes between ICH+EVs and ICH+Veh groups were not found at 24 h and 30 days, which may be due to the lack of effect of the injected EVs in the acute stage, and the difficulty of distinguishing between EV-mediated repair (ICH+EVs) and self-healing (ICH+Veh) in the chronic stage using 3.0T MRI.

An in-depth analysis of the therapeutic mechanism was performed by RNA-Seq in a mouse model of ICH following EVs treatment. Differential gene expression insight suggests the variations among the experimental groups, an indicative of the neuronal repair is reflected by the upregulated (e.g., Ntrk1 [30]) or downregulated (e.g., Nox1 [32]) genes in ICH model after EVs infusion. The biological implications of these differentially expressed genes were further elucidated through functional genomics analysis. Notably, GO and Reactome pathway analysis revealed that many immune response-related biological processes and immunomodulatory pathways were enriched in the ICH mice. Upon administration of EVs, processes related to divalent metal ion transport and neuronal system pathway were markedly enriched. This suggests a potential therapeutic role of MSC-EVs in modulating the metal ion and exhibiting neuroprotective efficacy in ICH. Moreover, GSEA further revealed enrichment of the metal ion solute carriers (SLC) transporters pathway in the ICH+EVs group, typified by the core enrichment of several *SLC* genes (*Slc41a2*, *Cp*, *Slc39a14*, et al.). Remarkably, it has been well-known that Cp and Slc39a14 are associated with the ferroptosis in stroke and other diseases [45, 46]. Overall, these results suggest that the therapeutic effects of MSC-EVs in ICH may be mediated through inhibition of ferroptosis and protection of the neuronal system. These findings provide valuable insights into the molecular mechanisms underlying the therapeutic efficacy of MSC-EVs in ICH and may guide the development of novel therapeutic strategies for ICH.

To clarify the neuroprotection of MSC-EVs on ICH, the typical pathology of ICH including oxidative stress and neuronal damage was examined in the present study as well. Our results showed a significant increase in the expression of Nrf2 and HO-1 proteins in the EV-treated mice compared to the ICH model, indicating that the administration of MSC-EVs contributes to the activation of the Nrf2/HO-1 pathway. Notably, this pathway is known to play a crucial role in cellular defense against oxidative stress [47]. Additionally, NOX2 is a key component of NADPH oxidase that generates reactive oxygen species and induces oxidative stress [48], and 8-OHdG is a well-established marker for oxidative DNA damage [49]. Our findings of reduced NOX2 and 8-OHdG expression following EV administration further corroborate the potential of MSC-EVs in mitigating oxidative stress. Thus, the activation of Nrf2/HO-1 system and reduction of oxidation in the ICH mice indicate the neuronal restoration contributed by EVs injection. In view of the significance of DAMPs in ICH [50, 51], the observed

reduction in the expression of DAMPs, namely HMGB1 and HSP70, in the ICH+EVs group further supports the neuroprotective potential of MSC-EVs, as well as the downregulation of neuroinflammation and related neuronal damage. Collectively, the results of this study suggest that the administration of MSC-EVs can alleviate the neuronal damage in cortical areas caused by ICH.

Since ferroptosis has been implicated the neuronal damage [6, 7, 52], and RNA-Seq indicates the involvement of metal ion transport after EV treatment in ICH mice. We further investigated the effects of EV therapy on Hemin-stimulated neuronal cells (a form of ICH model in vitro). Recent reports indicate that Hemin stimulation triggers ferroptosis, evidenced by an increase in Mito-FerroGreen staining (an iron ion fluorescence probe) and a decrease in GPX4 staining (a ferroptosis marker) [53]. Notably, the administration of MSC-EVs significantly reversed these neuronal changes induced by Hemin, suggesting that MSC-EVs have a protective effect against ferroptosis. This was further confirmed by the examination of neuronal ferroptosis, exemplified by an increase in ACSL4 expression and a decrease in GPX4 expression in ICH mice. Significantly, the indicative markers of reduced ferroptosis were reversed by the reversed changes of these markers in animal models following EVs administration. Interestingly, no significant effects of MSC-EVs were observed in the acute stage (24 h) and chronic stage (30 days), suggesting that MSC-EVs specifically counteract ferroptosis in ICH mice with a time window. Additionally, the general effect of MSC-EVs on ICH was negligible due to the lack of significant differences between Sham and Sham+EVs group. Moreover, as the mitochondrial alterations are markedly involved in the ferroptosis [35] we also used TEM to detect mitochondrial changes in the experimental groups. Notably, ICH-induced mitochondrial membrane swelling, outer membrane rupture, and others in cortical neurons were repaired by EVs injection, suggesting the inhibition of neuronal ferroptosis in ICH mice after MSC-EVs administration. Taken together, these findings suggest that MSC-EVs can alleviate neuronal ferroptosis both in vitro and in vivo.

Notably, EV-miRNAs are increasingly considered impactful molecular agents for the treatment of neurological disorders [18, 37]. In the present study, we found that MSC-EVs contained 289 miRNAs, the reliability of which was indicated by matching the majority to the Vesiclepedia data. Particularly, target gene prediction analysis showed that a suit of EV-miRNAs (8 miRNAs) could target ferroptosis mark genes like GPX4 and ACSL4, suggesting that these miRNAs are involved in the regulation of neuronal ferroptosis. In consideration of the high Tot score and low energy score of miR-760 and miRNA-124-3p in MSC-EVs, we further used corresponding miRNA inhibitor and mimics to treat Hemin-insulted neuronal cell line. The therapeutic effects of EV-miR-124-3p on neuronal ferroptosis were clarified by miRNA modification in an ICH cell model, indicating that miR-124-3p is a crucial therapeutic agent in MSC-EVs and plays an important regulatory role in neuronal ferroptosis. Notwithstanding, attention must be drawn to the fact that EVs (including MSC-EVs) harbor a plethora of functional miRNAs [36, 54].

However, there are several limitations to this study that need to be addressed. First, seven mice died during the experiments, four in the ICH+Veh group, two in the ICH+EVs group, and one in the model verification group, likely due to cerebral edema and subsequent brain herniation, as indicated by early MRI results. Second, no significant differences were found between the ICH+Veh and ICH+EVs groups on day 30, indicating the need for further research to ascertain the long-term effects and potential therapeutic window of MSC-EVs treatment for ICH. Future studies should employ high-resolution MRI (7.0 T or higher) to capture more precise and quantitative changes. Third, beyond the identified EV-miRNAs, a broader array of miRNAs likely modulates neuronal ferroptosis. Future investigations should incorporate non-functional EVs, such as those isolated from milk, as baseline comparators to delineate the specific roles of EV-miRNAs in neuronal ferroptosis.

Conclusions

In this study, we have unveiled a novel therapeutic potential and elucidate the underlying mechanisms of MSC-EVs in the treatment of ICH models. Specifically, we show that MSC-EVs are capable of traversing the BBB and homing to the affected cortical neurons, and these vesicles mitigate ICH-induced neuroimaging changes and neuronal injury. Through RNA-Seq analysis, the results suggest that EV-treatment modulates the neuronal system and metal ion transport pathways in the context of ICH. Moreover, our data indicate that MSC-EV administration can protect neurons from ferroptosis both in vitro and in vivo. We also identify miR-214-3p, contained within MSC-EVs, as a therapeutic molecule that regulates neuronal ferroptosis. Our findings advocate for the application of MSC-EVs as an effective therapeutic strategy to impede the progression of ICH pathogenesis and propose new avenues for the management of ferroptosis-linked neurological conditions. Future studies should aim to reproduce these findings in large animal models with advanced imaging surveillance to further validate and expand upon our results.

Abbreviations

8-OHdG	8-Hydroxy-Desoxyguanosine
ACSL4	Acyl Coenzyme A Synthetase Long Chain Family, Member 4
ANOVA	Analysis Of Variance

BBB	Blood-Brain Barrier
BCA	Bicinchoninic Acid
BP	Biological Processes
CC	Cellular Components
Cp	Ceruloplasmin
DAMPs	Damage-Associated Molecular Patterns
DWI	Diffusion-Weighted Imaging
EVs	extracellular vesicles
FBS	Fetal Bovine Serum
FPKM	Fragments Per Kilobase Of Exon Model Per Million Mapped Reads
GO	Gene Ontology
GPX4	Glutathione Peroxidase 4
GSEA	Gene Set Enrichment Analysis
HMGB1	High Mobility Group Protein 1
HO-1	Heme Oxygenase 1
HSP70	Heat Shock Protein 70
IL-25	Interleukin 25
ICH	Intracerebral Hemorrhage
MF	Molecular Functions
MRI	Magnetic Resonance Imaging
MSCs	Mesenchymal Stem Cells
NC	Negative Control
Nox	NADPH oxidase
Nrf2	Nuclear Factor Erythroid 2-Related Factor 2
Ntrk1	Neurotrophic Tyrosine Kinase Receptor type 1
NTA	Nanoparticle Tracking Analysis
PBS	Phosphate Buffer Saline
PFA	Paraformaldehyde
qPCR	Real Time Quantitative PCR
RNA-Seq	RNA Sequencing
SEM	Standard Error Of Mean
SLC	Solute Carriers
TEM	Transmission Electron Microscopy
T1WI	T1-Weighted Imaging
T2WI	T2-Weighted Imaging
Trh	Thyrotropin-releasing Hormone

Supplementary Information

The online version contains supplementary material available at https://doi.org/10.1186/s13287-024-03879-x.

Supplementary Material 1

Supplementary Material 2

Acknowledgements

We would like to acknowledge Beijing Novogene Co., Ltd. (H101SC21010217) and Shanghai Biotechnology Corporation (BC200088-1) for their invaluable contribution to the RNA sequencing and EV miRNA microarray. Specifically, the differential genes and enrichments among the experiments were provided by Novogene Co., Ltd., and the potential miRNAs that targeting ferroptosis was provided by Shanghai Biotechnology Corporation. We greatly appreciate their expertise and support that made this project possible. We also thank to the Xi'an Key Laboratory of Central Nervous System Disease and Academician Expert Workstation of Xi'an.

Author contributions

Y.Y.: Conceptualization, Methodology, Software, Writing - Original draft preparation. L.G.: Data curation, Methodology, Writing - Original draft preparation. J.X.: Conceptualization, Methodology, Software. X.L.: Methodology, Visualization, Investigation. H.Y.: Methodology, Visualization. Q.L.: Methodology, Investigation. F.X.: Methodology, Investigation. J.N.: Visualization, Software, Validation. P.M.: Methodology, Validation. X.T.: Methodology, Software. X.W.: Methodology, Validation. Q.L.: Supervision, Conceptualization, Writing - Reviewing and Editing.

Funding

The present study was supported by the National Natural Science Foundation of China (82171353, 81871084), Shaanxi Provincial Science Fund for Distinguished Young Scholars (2023-JC-JQ-69), Xi'an Talent Plan Project (XYAC210023), and Major Projects of Xi'an Medical Research (21YXYJ0020).

Data availability

All data supporting the findings of this study are available within the paper and its Supplementary Information. The RNA sequencing and miRNA microarray data supporting the results reported in this paper have been deposited in the NIH National Library of Medicine (accession number: PRJNA1138656) and Figshare (DOI: https://doi.org/10.6084/m9.figshare.26346451), respectively. The datasets generated and/or analyzed during the current study are available from the corresponding author on reasonable request.

Declarations

Ethics approval and consent to participate

Human umbilical cord tissue was obtained from five healthy full-term mothers after informed consent. All procedures were approved by the Ethics Committee of Xi'an Central Hospital, Xi'an Jiaotong University (Approved project: Extracellular Vesicle Biorepository, Approval No. LAS-L-2022-004-01, Date of approval: Mar 21, 2022), and complied with the standards of the National Health Research Institute. Umbilical cord guardians provided written informed consent for the use of samples. All animal procedures (Approved Project: Ethical Approval Document for Biological Research) were performed in accordance with the ARRIVE guidelines and approved by the Ethics Review Board of Xi'an Central Hospital, Xi'an Jiaotong University (Approval No.2021 – 1104, Date of approval, June 5, 2023).

Consent for publication

Not applicable.

Competing interests

The authors declare no competing financial interest.

Received: 1 May 2024 / Accepted: 5 August 2024
Published online: 13 August 2024

References

1. Magid-Bernstein J, Girard R, Polster S, Srinath A, Romanos S, Awad IA, et al. Cerebral hemorrhage: pathophysiology, treatment, and future directions. Circ Res. 2022;130:1204–29. https://doi.org/10.1161/circresaha.121.319949.
2. Qureshi AI, Mendelow AD, Hanley DF. Intracerebral haemorrhage. Lancet. 2009;373:1632–44. https://doi.org/10.1016/s0140-6736(09)60371-8.
3. van Asch CJ, Luitse MJ, Rinkel GJ, van der Tweel I, Algra A, Klijn CJ. Incidence, case fatality, and functional outcome of intracerebral haemorrhage over time, according to age, sex, and ethnic origin: a systematic review and meta-analysis. Lancet Neurol. 2010;9:167–76. https://doi.org/10.1016/s1474-4422(09)70340-0.
4. Aronowski J, Zhao X. Molecular pathophysiology of cerebral hemorrhage: secondary brain injury. Stroke. 2011;42:1781–6. https://doi.org/10.1161/strokeaha.110.596718.
5. Xiao Z, Shen D, Lan T, Wei C, Wu W, Sun Q, et al. Reduction of lactoferrin aggravates neuronal ferroptosis after intracerebral hemorrhagic stroke in hyperglycemic mice. Redox Biol. 2022;50:102256. https://doi.org/10.1016/j.redox.2022.102256.
6. Stockwell BR, Friedmann Angeli JP, Bayir H, Bush AI, Conrad M, Dixon SJ, et al. Ferroptosis: a regulated cell death Nexus linking metabolism, Redox Biology, and Disease. Cell. 2017;171:273–85. https://doi.org/10.1016/j.cell.2017.09.021.
7. Zille M, Karuppagounder SS, Chen Y, Gough PJ, Bertin J, Finger J, et al. Neuronal death after hemorrhagic stroke in Vitro and in vivo shares features of ferroptosis and Necroptosis. Stroke. 2017;48:1033–43. https://doi.org/10.1161/strokeaha.116.015609.
8. Witwer KW, Van Balkom BWM, Bruno S, Choo A, Dominici M, Gimona M, et al. Defining mesenchymal stromal cell (MSC)-derived small extracellular vesicles for therapeutic applications. J Extracell Vesicles. 2019;8:1609206. https://doi.org/10.1080/20013078.2019.1609206.
9. Cheng L, Hill AF. Therapeutically harnessing extracellular vesicles. Nat Rev Drug Discov. 2022;21:21. https://doi.org/10.1038/s41573-022-00410-w.

10. Palanisamy CP, Pei J, Alugoju P, Anthikapalli NVA, Jayaraman S, Veeraraghavan VP, et al. New strategies of neurodegenerative disease treatment with extracellular vesicles (EVs) derived from mesenchymal stem cells (MSCs). Theranostics. 2023;13:4138–65. https://doi.org/10.7150/thno.83066.
11. Rahmani A, Saleki K, Javanmehr N, Khodaparast J, Saadat P, Nouri HR. Mesenchymal stem cell-derived extracellular vesicle-based therapies protect against coupled degeneration of the central nervous and vascular systems in stroke. Ageing Res Rev. 2020;62:101106. https://doi.org/10.1016/j.arr.2020.101106.
12. Zou Y, Liao L, Dai J, Mazhar M, Yang G, Wang H, et al. Mesenchymal stem cell-derived extracellular vesicles/exosome: a promising therapeutic strategy for intracerebral hemorrhage. Regen Ther. 2023;22:181–90. https://doi.org/10.1016/j.reth.2023.01.006.
13. Yang G, Fan X, Mazhar M, Yang S, Xu H, Dechsupa N, et al. Mesenchymal stem cell application and its therapeutic mechanisms in Intracerebral Hemorrhage. Front Cell Neurosci. 2022;16:898497. https://doi.org/10.3389/fncel.2022.898497.
14. Bedini G, Bersano A, Zanier ER, Pischiutta F, Parati EA. Mesenchymal stem cell therapy in Intracerebral Haemorrhagic Stroke. Curr Med Chem. 2018;25:2176–97. https://doi.org/10.2174/0929867325666180111101410.
15. Otero-Ortega L, Gómez de Frutos MC, Laso-García F, Rodríguez-Frutos B, Medina-Gutiérrez E, López JA, et al. Exosomes promote restoration after an experimental animal model of intracerebral hemorrhage. J Cereb Blood Flow Metab. 2018;38:767–79. https://doi.org/10.1177/0271678x17708917.
16. Han Y, Seyfried D, Meng Y, Yang D, Schultz L, Chopp M, et al. Multipotent mesenchymal stromal cell-derived exosomes improve functional recovery after experimental intracerebral hemorrhage in the rat. J Neurosurg. 2018;131:290–300. https://doi.org/10.3171/2018.2.Jns171475.
17. Luo Q, Xian P, Wang T, Wu S, Sun T, Wang W, et al. Antioxidant activity of mesenchymal stem cell-derived extracellular vesicles restores hippocampal neurons following seizure damage. Theranostics. 2021;11:5986–6005. https://doi.org/10.7150/thno.58632.
18. Kuang Y, Zheng X, Zhang L, Ai X, Venkataramani V, Kilic E, et al. Adipose-derived mesenchymal stem cells reduce autophagy in stroke mice by extracellular vesicle transfer of miR-25. J Extracell Vesicles. 2020;10:e12024. https://doi.org/10.1002/jev2.12024.
19. Ge X, Guo M, Hu T, Li W, Huang S, Yin Z, et al. Increased Microglial Exosomal Mir-124-3p alleviates neurodegeneration and improves cognitive outcome after rmTBI. Mol Ther. 2020;28:503–22. https://doi.org/10.1016/j.ymthe.2019.11.017.
20. Phinney DG, Pittenger MF, Concise Review. MSC-Derived exosomes for cell-free therapy. Stem Cells. 2017;35:14. https://doi.org/10.1002/stem.2575.
21. Dominici M, Le Blanc K, Mueller I, Slaper-Cortenbach I, Marini F, Krause D, et al. Minimal criteria for defining multipotent mesenchymal stromal cells. The International Society for Cellular Therapy position statement. Cytotherapy. 2006;8:315–7. https://doi.org/10.1080/14653240600855905.
22. Chen J, Wang Y, Li M, Zhu X, Liu Z, Chen Q, et al. Netrin-1 alleviates early Brain Injury by regulating ferroptosis via the PPARγ/Nrf2/GPX4 signaling pathway following subarachnoid hemorrhage. Transl Stroke Res. 2024;15:219–37. https://doi.org/10.1007/s12975-022-01122-4.
23. Rynkowski MA, Kim GH, Komotar RJ, Otten ML, Ducruet AF, Zacharia BE, et al. A mouse model of intracerebral hemorrhage using autologous blood infusion. Nat Protoc. 2008;3:122–8. https://doi.org/10.1038/nprot.2007.513.
24. Gangadaran P, Hong CM, Oh JM, Rajendran RL, Kalimuthu S, Son SH, et al. In vivo non-invasive imaging of radio-labeled exosome-mimetics derived from Red Blood cells in mice. Front Pharmacol. 2018;9:817. https://doi.org/10.3389/fphar.2018.00817.
25. Xian P, Hei Y, Wang R, Wang T, Yang J, Li J, et al. Mesenchymal stem cell-derived exosomes as a nanotherapeutic agent for amelioration of inflammation-induced astrocyte alterations in mice. Theranostics. 2019;9:5956–75. https://doi.org/10.7150/thno.33872.
26. López-Romero P. Pre-processing and differential expression analysis of Agilent microRNA arrays using the AgiMicroRna Bioconductor library. BMC Genomics. 2011;12:64. https://doi.org/10.1186/1471-2164-12-64.
27. Long Q, Upadhya D, Hattiangady B, Kim DK, An SY, Shuai B, et al. Intranasal MSC-derived A1-exosomes ease inflammation, and prevent abnormal neurogenesis and memory dysfunction after status epilepticus. Proc Natl Acad Sci U S A. 2017;114:E3536–45. https://doi.org/10.1073/pnas.1703920114.
28. Théry C, Witwer KW, Aikawa E, Alcaraz MJ, Anderson JD, Andriantsitohaina R, et al. Minimal information for studies of extracellular vesicles 2018 (MISEV2018): a position statement of the International Society for Extracellular Vesicles and update of the MISEV2014 guidelines. J Extracell Vesicles. 2018;7:1535750. https://doi.org/10.1080/20013078.2018.1535750.
29. Jing C, Bian L, Wang M, Keep RF, Xi G, Hua Y. Enhancement of Hematoma Clearance with CD47 blocking antibody in experimental intracerebral hemorrhage. Stroke. 2019;50:1539–47. https://doi.org/10.1161/strokeaha.118.024578.
30. Yang K, Wu J, Li S, Wang S, Zhang J, Wang YP, et al. NTRK1 knockdown induces mouse cognitive impairment and hippocampal neuronal damage through mitophagy suppression via inactivating the AMPK/ULK1/FUNDC1 pathway. Cell Death Discov. 2023;9:404. https://doi.org/10.1038/s41420-023-01685-7.
31. Liu YY, Brent GA. The role of thyroid hormone in neuronal Protection. Compr Physiol. 2021;11:2075–95. https://doi.org/10.1002/cphy.c200019.
32. Dao VT, Elbatreek MH, Altenhöfer S, Casas AI, Pachado MP, Neullens CT, et al. Isoform-selective NADPH oxidase inhibitor panel for pharmacological target validation. Free Radic Biol Med. 2020;148:60–9. https://doi.org/10.1016/j.freeradbiomed.2019.12.038.
33. Lan X, Han X, Li Q, Yang QW, Wang J. Modulators of microglial activation and polarization after intracerebral haemorrhage. Nat Rev Neurol. 2017;13:420–33. https://doi.org/10.1038/nrneurol.2017.69.
34. Zhang H, Ostrowski R, Jiang D, Zhao Q, Liang Y, Che X, et al. Hepcidin Promoted Ferroptosis through Iron Metabolism which is Associated with DMT1 Signaling Activation in Early Brain Injury following subarachnoid hemorrhage. Oxid Med Cell Longev. 2021;2021:9800794. https://doi.org/10.1155/2021/9800794.
35. Xie X, Liu Y, Liu G, Zhao Y, Bian J, Li Y, et al. Photocontrollable Fluorescence Imaging of Mitochondrial Peroxynitrite during ferroptosis with High Fidelity. Anal Chem. 2022;94:10213–20. https://doi.org/10.1021/acs.analchem.2c01758.
36. Schulz-Siegmund M, Aigner A. Nucleic acid delivery with extracellular vesicles. Adv Drug Deliv Rev. 2021;173:89–111. https://doi.org/10.1016/j.addr.2021.03.005.
37. Mori MA, Ludwig RG, Garcia-Martin R, Brandão BB, Kahn CR. Extracellular miRNAs: from biomarkers to mediators of physiology and disease. Cell Metab. 2019;30:656–73. https://doi.org/10.1016/j.cmet.2019.07.011.
38. Liang Z, Zheng Z, Guo Q, Tian M, Yang J, Liu X, et al. The role of HIF-1α/HO-1 pathway in hippocampal neuronal ferroptosis in epilepsy. iScience. 2023;26:108098. https://doi.org/10.1016/j.isci.2023.108098.
39. Cheng L, Zhu X, Liu Y, Zhu K, Lin K, Li F. ACSL4 contributes to sevoflurane-induced ferroptotic neuronal death in SH-SY5Y cells via the 5′AMP-activated protein kinase/mammalian target of rapamycin pathway. Ann Transl Med. 2021;9:1454. https://doi.org/10.21037/atm-21-4249.
40. Cui LL, Kerkelä E, Bakreen A, Nitzsche F, Andrzejewska A, Nowakowski A, et al. The cerebral embolism evoked by intra-arterial delivery of allogeneic bone marrow mesenchymal stem cells in rats is related to cell dose and infusion velocity. Stem Cell Res Ther. 2015;6:11. https://doi.org/10.1186/scrt544.
41. Lino MM, Simões S, Tomatis F, Albino I, Barrera A, Vivien D, et al. Engineered extracellular vesicles as brain therapeutics. J Control Release. 2021;338:472–85. https://doi.org/10.1016/j.jconrel.2021.08.037.
42. Holm MM, Kaiser J, Schwab ME. Extracellular vesicles: Multimodal envoys in neural maintenance and repair. Trends Neurosci. 2018;41:360–72. https://doi.org/10.1016/j.tins.2018.03.006.
43. Boulouis G, van Etten ES, Charidimou A, Auriel E, Morotti A, Pasi M, et al. Association of Key Magnetic Resonance Imaging Markers of Cerebral Small Vessel Disease with Hematoma volume and expansion in patients with Lobar and Deep Intracerebral Hemorrhage. JAMA Neurol. 2016;73:1440–47. https://doi.org/10.1001/jamaneurol.2016.2619.
44. Rindler RS, Allen JW, Barrow JW, Pradilla G, Barrow DL. Neuroimaging Intracerebral Hemorrhage Neurosurg. 2020;86:E414–23. https://doi.org/10.1093/neuros/nyaa029.
45. Tuo QZ, Lei P, Jackman KA, Li XL, Xiong H, Li XL, et al. Tau-mediated iron export prevents ferroptotic damage after ischemic stroke. Mol Psychiatry. 2017;22:1520–30. https://doi.org/10.1038/mp.2017.171.
46. Yu Y, Jiang L, Wang H, Shen Z, Cheng Q, Zhang P, et al. Hepatic transferrin plays a role in systemic iron homeostasis and liver ferroptosis. Blood. 2020;136:726–39. https://doi.org/10.1182/blood.2019002907.
47. Haskew-Layton RE, Payappilly JB, Smirnova NA, Ma TC, Chan KK, Murphy TH, et al. Controlled enzymatic production of astrocytic hydrogen peroxide protects neurons from oxidative stress via an Nrf2-independent pathway. Proc Natl Acad Sci U S A. 2010;107:17385–90. https://doi.org/10.1073/pnas.1003996107.
48. Fan LM, Geng L, Cahill-Smith S, Liu F, Douglas G, McKenzie CA, et al. Nox2 contributes to age-related oxidative damage to neurons and the cerebral

vasculature. J Clin Invest. 2019;129:3374–86. https://doi.org/10.1172/jci125173.
49. Omari Shekaftik S, Nasirzadeh N. 8-Hydroxy-2′-deoxyguanosine (8-OHdG) as a biomarker of oxidative DNA damage induced by occupational exposure to nanomaterials: a systematic review. Nanotoxicology. 2021;15:850–64. https://doi.org/10.1080/17435390.2021.1936254.
50. Wang D, Liu K, Wake H, Teshigawara K, Mori S, Nishibori M. Anti-high mobility group box-1 (HMGB1) antibody inhibits hemorrhage-induced brain injury and improved neurological deficits in rats. Sci Rep. 2017;7:46243. https://doi.org/10.1038/srep46243.
51. Shao A, Zhou Y, Yao Y, Zhang W, Zhang J, Deng Y. The role and therapeutic potential of heat shock proteins in haemorrhagic stroke. J Cell Mol Med. 2019;23:5846–58. https://doi.org/10.1111/jcmm.14479.
52. Ren S, Chen Y, Wang L, Wu G. Neuronal ferroptosis after intracerebral hemorrhage. Front Mol Biosci. 2022;9:966478. https://doi.org/10.3389/fmolb.2022.966478.
53. Chen J, Wang Y, Li M, Zhu X, Liu Z, Chen Q, et al. Netrin-1 alleviates early Brain Injury by regulating ferroptosis via the PPARγ/Nrf2/GPX4 signaling pathway following subarachnoid hemorrhage. Transl Stroke Res. 2023. https://doi.org/10.1007/s12975-022-01122-4.
54. Kosaka N, Iguchi H, Yoshioka Y, Takeshita F, Matsuki Y, Ochiya T. Secretory mechanisms and intercellular transfer of microRNAs in living cells. J Biol Chem. 2010;285:17442–52. https://doi.org/10.1074/jbc.M110.107821.

Publisher's Note